Pergamon

Int. J. Solids Structures Vol. 34, No. 7, pp. 769–787, 1997

0020-7683/97 $17.00 + .00

PII: S0020-7683(96)00062-5

A NUMERICAL STUDY OF DYNAMIC CRACK GROWTH IN ELASTIC-VISCOPLASTIC SOLIDS

T. SIEGMUND and A. NEEDLEMAN
Division of Engineering, Box D, Brown University, Providence, RI, 02912, U.S.A.

(*Received* 20 *December* 1995, *in revised form April* 24, 1996)

Abstract—Dynamic crack growth is analyzed numerically for a plane strain block with an initial central crack subject to impact tensile loading. The material is characterized as an isotropically hardening elastic-viscoplastic solid. A cohesive surface constitutive relation is also specified that relates the tractions and displacement jumps across the crack plane. In this formulation crack initiation, crack growth and crack arrest emerge naturally as outcomes of the imposed loading, without any ad hoc assumptions concerning crack growth criteria. Full transient analyses are carried out using two characterizations of strain rate hardening; power law strain rate hardening and a combined power law–exponential relation that gives rise to enhanced strain rate hardening at high strain rates. The effects of the strain rate hardening characterization on crack initiation, crack growth and crack arrest are investigated. Enhanced strain rate hardening is found to lead to higher crack speeds, to lower toughness values and to crack tip fields that are more like those of an elastic solid than for the power law rate hardening solid. Additionally, some parameter studies varying the cohesive surface strength and the material flow strength are carried out. The effective stress intensity factor is found to increase dramatically at a certain value of the crack speed that depends on the cohesive surface strength, the material flow strength, the characterization of strain rate hardening and the impact velocity, but there is a range where the crack speed at which the increase in effective stress intensity factor occurs is not very sensitive to impact velocity.

1. INTRODUCTION

Rather few solutions are available for the transient growth of tensile cracks in inelastic solids. Analyses of fast crack growth in structural metals have generally either assumed a steady state, e.g., Lam and Freund (1985), Varias and Shih (1994), or have been based on an approach where a material and crack speed dependent value of a characterizing parameter, such as the energy release rate or the stress intensity factor, is used in conjunction with a crack tip equation of motion, Freund (1990), e.g., Brickstad and Nilsson (1980), Lee and Prakash (1995). Another approach involves incorporating detailed physically based models of the micromechanisms of failure into the material's constitutive description, as, for example, in Needleman and Tvergaard (1991) and Tvergaard and Needleman (1993).

Here, a phenomenological approach is adopted, where the fracture characteristics of the material are embedded in a cohesive surface traction–displacement separation relation, Needleman (1987). This cohesive surface framework has been used previously to model quasi-static crack growth in plastically deforming solids, e.g., Needleman (1990a, b), Tvergaard and Hutchinson (1992), and dynamic crack growth in elastic solids, e.g., Xu and Needleman (1994). Crack initiation, crack growth and crack arrest emerge naturally as outcomes of the imposed loading and are calculated directly in terms of the properties of the material and of the parameters characterizing the cohesive surface separation law. The cohesive parameters include a strength and the work of separation per unit area so that, from dimensional considerations, a characteristic length enters the formulation.

Full finite strain transient analyses are carried out for a plane strain block with an initial central crack, subject to tensile impact loading. The constitutive relation for the block material is that of an isotropic hardening elastic-viscoplastic solid. Two characterizations of the material strain rate sensitivity are considered. In some calculations, a pure power law relation is used, while in others the enhanced strain rate sensitivity exhibited by many metals at high strain rates, e.g., Campbell and Ferguson (1970), Klopp *et al.* (1985), is modeled. In all calculations, attention is confined to a single cohesive surface, which restricts

the crack to grow along the initial crack line. The material and cohesive parameters are chosen to give deformation behavior and toughness values representative of a structural steel.

The effect of enhanced strain rate hardening at high strain rates has been studied by Freund and Hutchinson (1985) and Mataga *et al.* (1987) assuming steady state growth and small scale yielding. These studies indicate that the enhanced strain rate sensitivity at high strain rates can play a significant role in the macroscopic ductile–brittle transition. The numerical, full field transient solutions obtained here exhibit, in detail, the role that high strain rate plasticity plays in limiting attainable crack speeds and in setting the amount of dissipation accompanying crack growth.

2. FORMULATION

The cohesive surface formulation and numerical method follow that in Xu and Needleman (1994). The difference here is that the material is taken to be elastic-viscoplastic and attention is confined to a single cohesive surface. A finite strain Lagrangian formulation is used, with the initial undeformed configuration taken as reference, so that all field quantities are considered to be functions of convected coordinates, y^i, which serve as particle labels, and time t. The principle of virtual work is written as

$$\int_V \mathbf{s}:\delta\mathbf{F}\,dV-\int_{S_{int}} \mathbf{T}\cdot\delta\boldsymbol{\Delta}\,dS=\int_{S_{ext}} \mathbf{T}\cdot\delta\mathbf{u}\,dS-\int_V \rho\frac{\partial^2\mathbf{u}}{\partial t^2}\cdot\delta\mathbf{u}\,dV \tag{1}$$

where $\mathbf{s}$ is the nonsymmetric nominal stress tensor, $\mathbf{u}$ is the displacement vector, $\mathbf{F}$ is the deformation gradient, $\boldsymbol{\Delta}$ is the displacement jump across the cohesive surface, $\mathbf{A}:\mathbf{B}$ denotes $A^{ij}B_{ji}$, V, S_{ext} and S_{int} are the volume, external surface area and internal cohesive surface area, respectively, of the body in the reference configuration. The density of the material in the reference configuration is ρ and the traction vector $\mathbf{T}$ and the reference configuration normal $\mathbf{n}$ are related by $\mathbf{T}=\mathbf{n}\cdot\mathbf{s}$. Also, $\mathbf{s}=\mathbf{F}^{-1}\cdot\boldsymbol{\tau}$, where $\boldsymbol{\tau}$ is the Kirchhoff stress, $\boldsymbol{\tau}=\det(\mathbf{F})\boldsymbol{\sigma}$, with $\boldsymbol{\sigma}$ being the Cauchy stress.

Computations are carried out for center cracked specimens, with initial height $2L$, initial width $2w$ and an initial crack of length $2a_i$ along $y^2=0$, as sketched in Fig. 1. We confine attention to specimens having $L=30$ mm, $w=30$ mm and an initial crack length of $a_i=10$ mm. Plane strain conditions are assumed to prevail and a Cartesian coordinate system is used as reference, with the y^1-y^2 plane as the plane of deformation.

At $t=0$, the body is stress free and at rest. Equal and opposite normal velocities are prescribed on the edges at $y^2=\pm L$, with the shear traction required to vanish. The edges

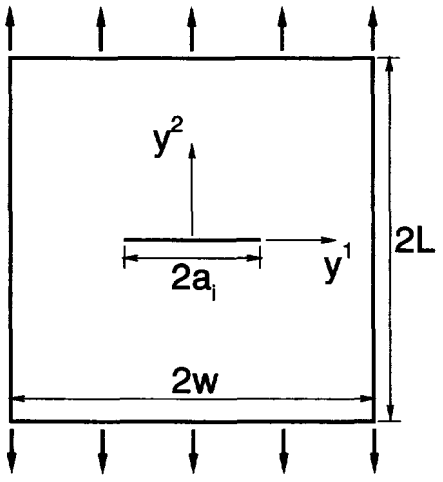

Fig. 1. Geometry of the center cracked specimen.

at $y^1 = \pm w$ are traction free. The cohesive surface lies on $y^2 = 0$ and $|y^1| > a_i$, with the initial crack specified by

$$T^1 = 0, T^2 = 0 \quad \text{on} \quad y^2 = 0 \quad \text{and} \quad -a_i \leqslant y^1 \leqslant a_i. \tag{2}$$

Symmetry conditions are presumed so that only one quarter of the specimen is analyzed numerically and the remaining boundary conditions are

$$u_1 = 0, T^2 = 0 \quad \text{on} \, y^1 = 0 \tag{3}$$

$$T^1 = 0, T^2 = 0 \quad \text{on} \, y^1 = w \tag{4}$$

$$u_2 = \int V(t)\,\mathrm{d}t, T^1 = 0 \quad \text{on} \, y^2 = L \tag{5}$$

where in (5)

$$V(t) = \begin{cases} V_1 t/t_r, & \text{for } t \leqslant t_r; \\ V_1, & \text{for } t > t_r. \end{cases} \tag{6}$$

The volumetric constitutive law is that of an elastic-viscoplastic isotropic hardening solid. Any effects of the temperature rise accompanying plastic dissipation are neglected and an isothermal constitutive relation is used. The total rate of deformation, $\mathbf{D} = \mathrm{sym}(\dot{\mathbf{F}} \cdot \mathbf{F}^{-1})$, is written as the sum of an elastic part, $\mathbf{D}^e$, and a plastic part $\mathbf{D}^p$ so that

$$\mathbf{D} = \mathbf{D}^e + \mathbf{D}^p. \tag{7}$$

Small elastic strains and elastic isotropy are presumed so that

$$\mathbf{D}^e = \mathscr{L}^{-1} : \hat{\boldsymbol{\tau}} \tag{8}$$

with $\hat{\tau}$ the Jaumann rate of Kirchhoff stress and

$$\mathscr{L} = \frac{E}{1+\nu}\left[\mathbf{I}' + \frac{\nu}{1-2\nu}\mathbf{I} \otimes \mathbf{I}\right] \tag{9}$$

where E is the Young's modulus, ν is Poisson's ratio, $\mathbf{I}$ and $\mathbf{I}'$ are the second and fourth order identity tensors, respectively, and $\otimes$ denotes the tensor product, $(\mathbf{A} \otimes \mathbf{B})^{ijkl} = A^{ij}B^{kl}$.

The speeds of dilatational, shear and Rayleigh surface waves are, e.g., Freund (1990),

$$c_d = \sqrt{\frac{E(1-\nu)}{\rho(1+\nu)(1-2\nu)}}, \quad c_s = \sqrt{\frac{E}{2\rho(1+\nu)}}, \quad c_R = c_s \frac{0.862+1.14\nu}{1+\nu}. \tag{10}$$

The viscoplastic flow law is

$$\mathbf{D}^p = \frac{3\dot{\bar{\varepsilon}}}{2\bar{\sigma}}\boldsymbol{\tau}' \tag{11}$$

where the effective plastic strain rate $\dot{\bar{\varepsilon}}$ is

$$\dot{\bar{\varepsilon}} = \sqrt{\tfrac{2}{3}\mathbf{D}^p : \mathbf{D}^p} \tag{12}$$

and

$$\tau' = \tau - \tfrac{1}{3}(\tau : \mathbf{I})\mathbf{I}, \bar{\sigma}^2 = \tfrac{3}{2}\tau' : \tau' \tag{13}$$

$$\dot{\bar{\varepsilon}} = R(\bar{\sigma}/g(\bar{\varepsilon})), g(\bar{\varepsilon}) = \sigma_0(\bar{\varepsilon}/\varepsilon_0 + 1)^N, \varepsilon_0 = \sigma_0/E. \tag{14}$$

Here, a superposed dot denotes differentiation with respect to time, $\bar{\varepsilon} = \int \dot{\bar{\varepsilon}}\, dt$, σ_0 is a reference flow strength, N is the strain hardening exponent and $R(\,)$ is a strain rate hardening function. Thermal softening is not accounted for in (14).

In some computations, R is taken to be a pure power law, i.e.,

$$R(x) = \dot{\varepsilon}_1(x) = \dot{\varepsilon}_0 x^{1/m} \tag{15}$$

where $\dot{\varepsilon}_0$ is a reference strain rate and m is the strain rate hardening exponent. In other calculations, the increased rate sensitivity at high strain rates is accounted for. Then, as in Zhou *et al.* (1994),

$$R(x) = \frac{\dot{\varepsilon}_1(x)\dot{\varepsilon}_2(x)}{\dot{\varepsilon}_1(x) + \dot{\varepsilon}_2(x)} \tag{16}$$

with $\dot{\varepsilon}_1(x)$ given by (15) and

$$\dot{\varepsilon}_2(x) = \dot{\varepsilon}_m \exp\left[-\frac{a}{x}\right]. \tag{17}$$

The form (16) provides a smooth transition between a power law at low strain rates (15) and an exponential relation at high strain rates (16), as shown in Fig. 2. The exponential relation gives rise to an enhanced strain rate sensitivity at high strain rates that is representative of the behavior found experimentally in mild steels by Campbell and Ferguson (1970). Subsequently, materials characterized by (15) will be referred to as power law strain rate hardening materials and materials characterized by (16) as materials with enhanced strain rate hardening.

The material properties are taken to be representative of a structural steel with $E = 211$ GPa, $\nu = 0.3$, $\sigma_0 = 1500, 1000, 857$ MPa, $N = 0.1$, $m = 0.01$, $\dot{\varepsilon}_0 = 1/\text{s}$, $\dot{\varepsilon}_m = 5 \times 10^7/\text{s}$, $a = 10$

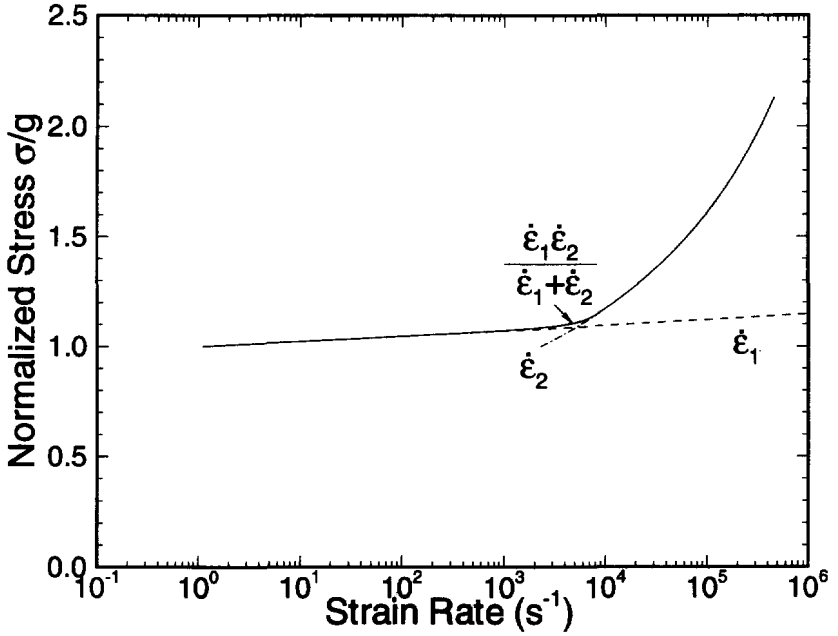

Fig. 2. Dependence of the normalized flow strength, $\bar{\sigma}/g$, on plastic strain rate, $\dot{\bar{\varepsilon}}$.

and $\rho = 7800\,\text{kg/m}^3 = 7.8 \times 10^{-3}\,\text{MPa/(m/s)}^2$. From (10), the dilational, shear and Rayleigh wave speeds are 6034 m/s, 3226 m/s and 2987 m/s, respectively. With this choice of parameters the transition from power law strain rate hardening to enhanced strain rate hardening takes place at a strain rate of about 5×10^3/s.

The constitutive law for the cohesive surface is taken to be elastic so that any dissipation associated with separation is neglected. The traction across the cohesive surface, which lies on $y^2 = 0$ and $|y^1| > a_i$, is given by

$$T_n = -\frac{\partial \phi}{\partial \Delta_n}. \tag{18}$$

Because the crack is constrained to grow along the initial crack line and symmetry conditions prevail about that line, only normal separation occurs. The specific form used for the potential, ϕ, is the exponential function of Rose *et al.* (1981)

$$\phi = \phi_n - \phi_n\left(1 + \frac{\Delta_n}{\delta_n}\right)\exp\left(-\frac{\Delta_n}{\delta_n}\right) \tag{19}$$

where ϕ_n is the work of normal separation, $\Delta_n = 2u_2(y^1, 0)$ is the normal displacement jump across the cohesive surface and δ_n is the cohesive characteristic length. Figure 3 shows the normal traction across the cohesive surface obtained from (19), T_n, as a function of Δ_n. At $\Delta_n = \delta_n$, the magnitude of the traction across the cohesive surface attains a maximum, σ_{max}. The work of separation, the cohesive surface strength and the cohesive surface characteristic length are related by

$$\phi_n = \exp(1)\sigma_{max}\,\delta_n. \tag{20}$$

When δ_n is substantially smaller than all geometric lengths, crack growth predictions are not sensitive to the shape of the potential, Needleman (1990a). In the calculations here, the cohesive surface characteristic length is fixed at $\delta_n = 2$ μm; the cohesive strength, σ_{max}, and consequently the work of separation, ϕ_n, are varied.

Under dynamic loading conditions the J-integral, Rice (1968), involves an area integral as well as a line integral, Nakamura *et al.* (1985),

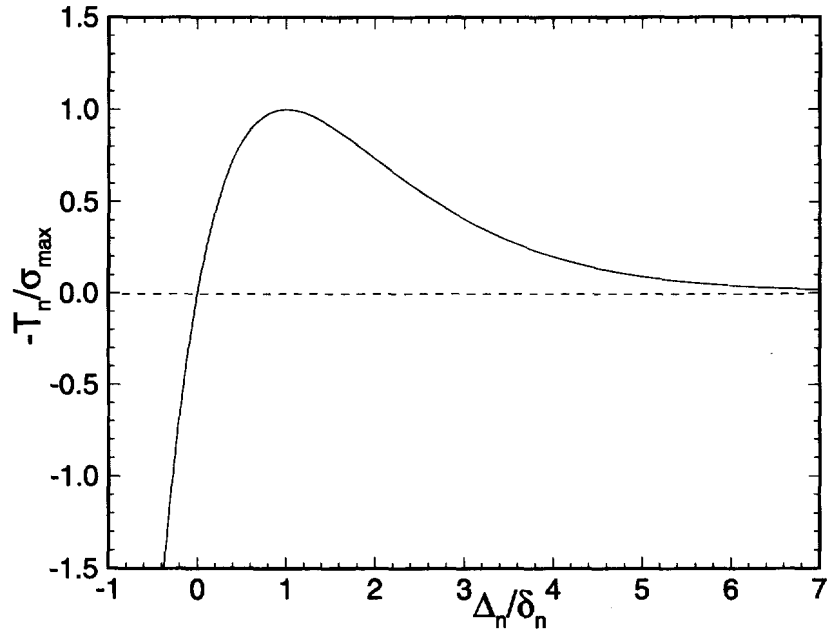

Fig. 3. Normalized normal traction, T_n/σ_{max}, across the cohesive surface as a function of Δ_n/δ_n.

Fig. 4. Finite element mesh near the initial crack tip.

$$J = \int_\Gamma \left[(W+L)n_1 - \mathbf{T}\cdot\frac{\partial \mathbf{u}}{\partial y^1} \right] ds + \int_A \left[\rho \frac{\partial \mathbf{v}}{\partial t}\cdot\frac{\partial \mathbf{u}}{\partial y^1} - \rho \mathbf{v}\cdot\frac{\partial \mathbf{v}}{\partial y^1} \right] dA \tag{21}$$

where $\mathbf{v} = \partial \mathbf{u}/\partial t$, $W = \int \boldsymbol{\tau} : \mathbf{D}\, dt$, $L = \rho \mathbf{v}\cdot\mathbf{v}/2$, Γ is a path surrounding the crack tip and n_1 is the component of the normal to Γ in the y^1-direction.

The finite element discretization is based on linear displacement triangular elements that are arranged in a 'crossed-triangle' quadrilateral pattern. The finite element mesh consists of 13,500 quadrilateral elements, with a uniform region ahead of the initial crack surrounded by a graduated mesh out to the specimen boundaries. The uniform region has 200×10 square elements, with side length 0.02 mm, as shown in Fig. 4. The equations resulting from substituting the finite element discretization into (1) are of the form

$$\mathbf{M}\frac{\partial^2 \mathbf{U}}{\partial t^2} = \mathbf{R} \tag{22}$$

where $\mathbf{M}$ is a mass matrix, $\mathbf{U}$ is the nodal displacement vector and $\mathbf{R}$ is the nodal force vector. The equations of motion (22) are integrated numerically by an explicit integration procedure, the Newmark β-method with $\beta = 0$, Belytschko *et al.* (1976). A lumped mass matrix is used instead of the consistent mass matrix, since this has been found preferable for explicit time integration procedures, from the point of view of accuracy as well as computational efficiency, Krieg and Key (1973). The constitutive updating is based on the rate tangent modulus method of Peirce *et al.* (1984).

3. RESULTS

Figure 5 shows the effect of varying the flow strength, σ_0, with the cohesive strength fixed at $\sigma_{max} = 3000$ MPa and with an impact velocity, V_1, of 10 m/s. The material strain rate sensitivity is taken to be characterized by the power law relation (15). The ratios σ_{max}/σ_0 equal to 2.0, 3.0 and 3.5 correspond to flow strengths of 1500 MPa, 1000 MPa and 857 MPa, respectively. For comparison purposes, results of a calculation with elastic material behavior, $\mathbf{D}^p \equiv 0$ in (7), are also shown and denoted by $\sigma_{max}/\sigma_0 = 0$.

The first loading wave arrives at the crack tip at 4.98 μs after impact and the next loading wave at 14.94 μs. The plastic deformation associated with the impact is negligible so that the stress carried by the loading wave is given by $\rho c_d V_1$. An impact velocity of 10 m/s then corresponds to a stress level of 470 MPa. However, because there is impact at both ends, the stress level on the crack plane when the first loading wave arrives is 940 MPa.

Curves of crack speed, $\dot{a}$, vs time are shown in Fig. 5a. The crack location is identified with $\Delta_n \geqslant 5\,\delta_n$ and the curve of crack location vs time is differentiated as described in Xu and Needleman (1994) to obtain the crack speed. There is a delay between the arrival of the loading wave and the initiation of crack growth that increases with decreasing flow strength. The calculations are terminated when the crack approaches the end of the uniform mesh region. When the material behavior is elastic, the crack speed increases monotonically. With $\sigma_{max}/\sigma_0 = 2.0$, the crack speed vs time curve is identical to that for the corresponding elastic solid in the early stages of crack growth, but subsequently the crack speed is somewhat slower. In this case, the initiation of crack growth precedes the development of significant plastic deformation. When σ_{max}/σ_0 is increased to 3.0, the delay between the

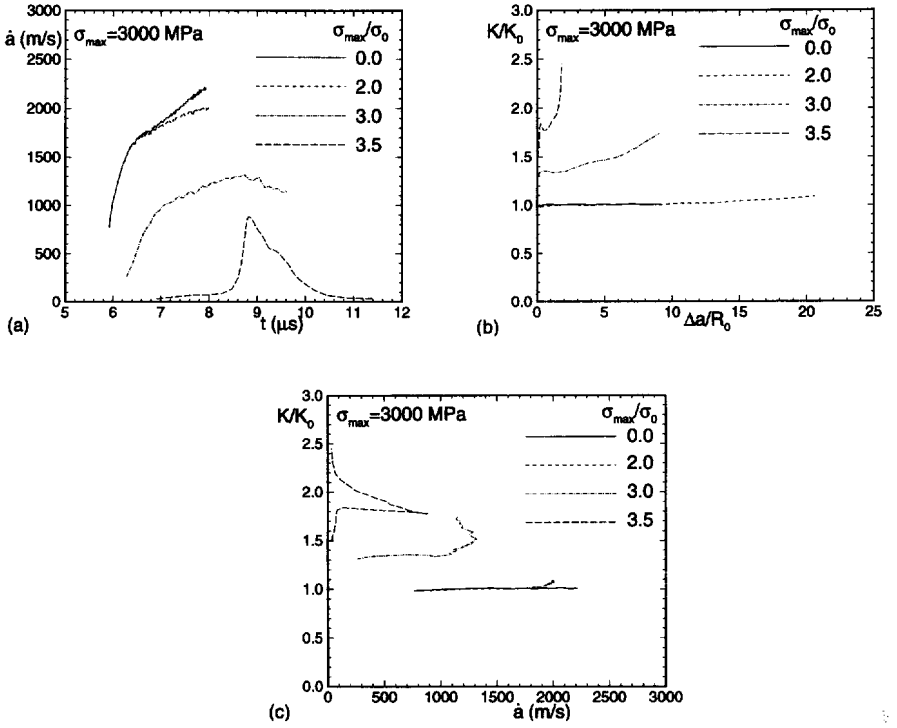

Fig. 5. Comparison of the crack growth behavior for various ratios σ_{max}/σ_0, σ_{max} = 3000 MPa and power law strain rate hardening, (15). The impact velocity is V_1 = 10 m/s. (a) Crack speed, $\dot{a}$, vs time, t. (b) Normalized stress intensity factor, K/K_0, vs normalized crack growth, $\Delta a/R_0$. (c) Normalized stress intensity factor, K/K_0, vs crack speed $\dot{a}$. A value R_0 = 0.40 mm is used for normalizing the results of the calculation with elastic material behavior.

arrival of the loading wave and the onset of crack growth increases somewhat, and plastic flow precedes the onset of crack growth. With $\sigma_{max}/\sigma_0 = 3.5$, the onset of significant crack growth is further delayed, until ≈ 8.5 μs. For the calculations with $\sigma_{max}/\sigma_0 = 3.0$ and $\sigma_{max}/\sigma_0 = 3.5$, the crack speeds exhibit a local maximum. In Siegmund and Needleman (1996), it was found that the time at which the maximum crack speed is attained depends on impact velocity. Hence, the crack speed maximum is not a consequence of wave effects. For $\sigma_{max}/\sigma_0 = 3.0$, the crack speed reaches a maximum of 1315 m/s at 8.74 μs and then decreases. With $\sigma_{max}/\sigma_0 = 3.5$ the crack speed reaches a maximum of 884 m/s at 8.82 μs and the crack subsequently arrests.

Figure 5b shows curves of normalized stress intensity factor, K/K_0, vs the normalized amount of crack growth, $\Delta a/R_0$. Here, K is defined in terms of the J-integral in (21) by

$$K = \sqrt{\frac{EJ}{(1-\nu^2)}}. \tag{23}$$

The results are presented in terms of K (23), which is the stress intensity factor in small scale yielding, in order to make contact with previous work. In all calculations here, except for some cases in Fig. 6 with increased impact velocity, plastic deformation is confined to a region near the tip that is small compared with the overall specimen dimensions. Using (21), J was calculated on several contours outside the uniformly spaced mesh region, with any contribution of the cohesive surface ignored. The deviation on all paths away from the uniform mesh region was within 5%, with the deviation being less in the early stages of crack growth.

Additionally, the reference quantities

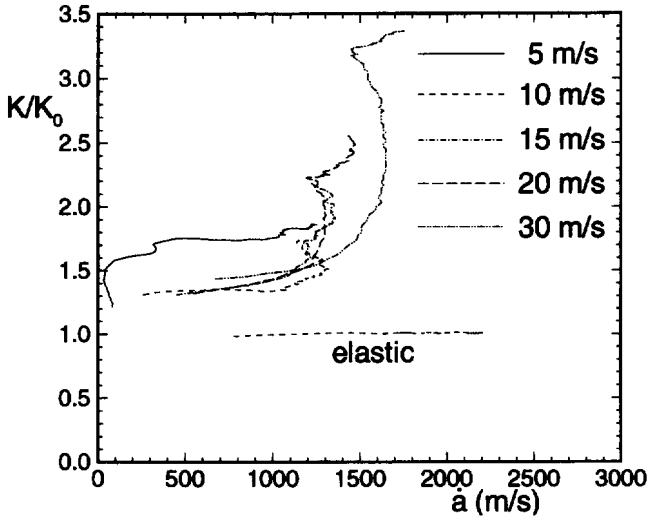

Fig. 6. Normalized stress intensity factor, K/K_0, vs crack speed, $\dot{a}$, with $\sigma_{max} = 3000$ MPa, $\sigma_0 = 1000$ MPa and power law strain rate hardening, (15), for various values of the impact velocity, $V_1 = 5$, 10, 15, 20 and 30 m/s. For comparison purposes, results from a calculation with elastic material behavior, $V_1 = 10$ m/s and $\sigma_{max} = 3000$ MPa are also shown.

$$K_0 = \sqrt{\frac{E\phi_n}{(1-\nu^2)}} \quad R_0 = \frac{1}{3\pi}\left(\frac{K_0}{\sigma_0}\right)^2 \tag{24}$$

are used for normalization to facilitate comparison with the quasi-static results in Tvergaard and Hutchinson (1992). The quantity K_0 defines a reference stress intensity factor and R_0 is a reference plastic zone size. With $\sigma_{max} = 3000$ MPa, K_0 is 61 MPa$\sqrt{\text{m}}$. The value of R_0 varies with σ_0; for $\sigma_0 = 1500$ MPa, $R_0 = 0.18$ mm; for $\sigma_0 = 1000$ MPa, $R_0 = 0.40$ mm, and with $\sigma_0 = 857$ MPa, $R_0 = 0.54$ mm.

In the calculations, the value of the work of separation, ϕ_n, is fixed and any elevation of K above K_0 in Fig. 5b is a consequence of plastic dissipation. For the elastic solid, the crack speed is well below the Rayleigh wave speed over the range computed and crack growth occurs with $K/K_0 = 1.0$. With $\sigma_{max}/\sigma_0 = 2.0$, the value of K increases slightly above K_0 in the latter stages of crack growth only. With $\sigma_{max}/\sigma_0 = 3.0$ and 3.5, there is significant plastic deformation before the onset of crack growth, which gives an apparent increase in the value of K at initiation. This initiation value of K is sensitive to the value of Δ_n used to define the crack location. However, once significant crack growth takes place the sensitivity to this choice of crack location disappears. With $\sigma_{max}/\sigma_0 = 3.0$, the value of K increases rapidly in the early stages of crack growth, reaches a plateau and then increases again. For this case, the K/K_0 level in the range $\Delta a/R_0 \leqslant 2$, is in good agreement with the corresponding quasi-static result in Tvergaard and Hutchinson (1992). For the case with $\sigma_{max}/\sigma_0 = 3.5$, the value of K necessary for crack initiation is considerably higher than for $\sigma_{max}/\sigma_0 = 3.0$. Additionally, K increases even further during crack arrest, leading to the rapid rise in Fig. 5b.

The data from Figs 5a and 5b are used to plot curves of K/K_0 vs crack speed in Fig. 5c. For the calculation with $\sigma_{max}/\sigma_0 = 3.0$, this curve shows a strong upturn in the stress intensity factor at a crack speed of about 1200 m/s. This type of dependence of the stress intensity factor on crack speed is consistent with experimental observations, see, e.g., Rosakis and Zehnder (1985) and Zehnder and Rosakis (1990). With viscoplastic material behavior, the combination of material inertia and dissipation act to limit the attainable crack speed even when the crack is constrained to grow along the initial crack line. For the higher flow strength case, $\sigma_{max}/\sigma_0 = 2.0$, the upturn in K/K_0 occurs at a higher crack speed, $\dot{a} \approx 1800$ m/s, and for the elastic material behavior the curve is essentially flat. The tougher the material (the higher the value of the ratio σ_{max}/σ_0) the lower the crack speed at which the upturn in the stress intensity factor occurs. Similarly, Mataga *et al.* (1987) in their

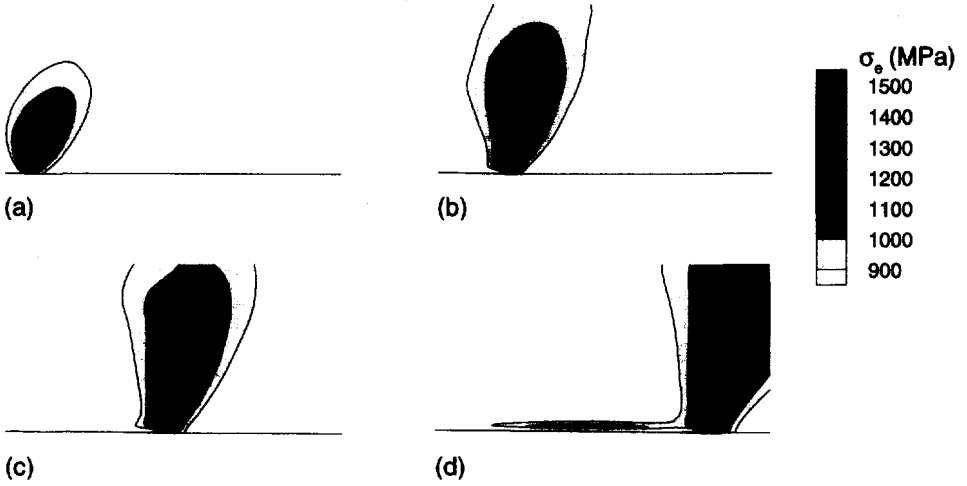

Fig. 7. Contours of Mises effective stress, σ_e, with $\sigma_{max} = 3000$ MPa, $\sigma_0 = 1000$ MPa and power law strain rate hardening, (15). The impact velocity is $V_1 = 10$ m/s. The extent of the region shown is 4 mm × 2 mm. (a) $t = 6.0$ μs, $\dot{a} = 0$ m/s. (b) $t = 7.0$ μs, $\dot{a} = 969$ m/s. (c) $t = 8.0$ μs, $\dot{a} = 1217$ m/s. (d) $t = 9.1$ μs, $\dot{a} = 1233$ m/s.

steady-state analysis using a strain-based growth criterion found that higher critical strains gave lower crack speeds for the upturn in the stress intensity factor.

It is worth noting that for the case where crack arrest occurs in Fig. 5c, the stress intensity factor at arrest is significantly larger that the one needed to initiate crack growth, although $\dot{a} = 0$ both at initiation and arrest.

Figure 6, which was also presented in Siegmund and Needleman (1996), shows the effect of varying the impact velocity on the curve of K/K_0 vs crack speed. While there clearly is not a one-to-one correspondence between the value of K/K_0 and the crack speed, three cases, those with impact velocities of 10 m/s, 15 m/s and 20 m/s, fall within a fairly narrow band. For these cases, the crack speed at which the sharp increase in K/K_0 takes place, ≈ 1200 m/s, is in good agreement with the experimental values in Rosakis and Zehnder (1985) and Zehnder and Rosakis (1990).

Contours of Mises effective stress are shown in Fig. 7 for the calculation with $\sigma_{max} = 3000$ MPa, $\sigma_0 = 1000$ MPa and $V_1 = 10$ m/s. The contour plots in this study were obtained using the commercial plotting program Tecplot from Amtec Engineering Inc., Bellevue, WA. This contouring program uses nodal values of field quantities, which are obtained by extrapolation from the element integration points to the nodal points. The extrapolated values associated with all elements connected to a node are then averaged. The first stage shown, $t = 6.0$ μs, is before the initiation of crack growth (see Fig. 5a). The next two stages, $t = 7.0$ μs and $t = 8.0$ μs, are during crack growth, but prior to the maximum crack speed being reached. At $t = 9.1$ μs the crack speed is decreasing. A region of high Mises effective stress behind the current crack tip begins to form in Fig. 7c. In Fig. 7d, the extent of this region has increased greatly. The growth of this region is associated with the attainment of a maximum crack speed.

The effect of the enhanced strain rate hardening, (16), is shown in Fig. 8, for the case with $\sigma_0 = 1000$ MPa and $\sigma_{max}/\sigma_0 = 3.0$. For comparison purposes, the results for the elastic solid are also shown in this figure. Compared with the corresponding power law rate hardening case in Fig. 5, the crack speed is increased, Fig. 8a, the effective stress intensity factor, K, is reduced, Fig. 8b, and the upturn in the stress intensity–crack speed response occurs at a higher crack speed, Fig. 8c. The contours of Mises effective stress in Fig. 9 show that a region of enhanced Mises effective stress behind the crack tip does not develop in this case.

Contours of Mises effective stress, for the same amount of crack growth, are compared in Fig. 10 for three cases; power law strain rate hardening, Fig. 10a; enhanced strain rate hardening, Fig. 10b; and an elastic material, Fig. 10c. Although all three cases correspond to the same amount of crack growth, the times and the crack speeds differ. The contours

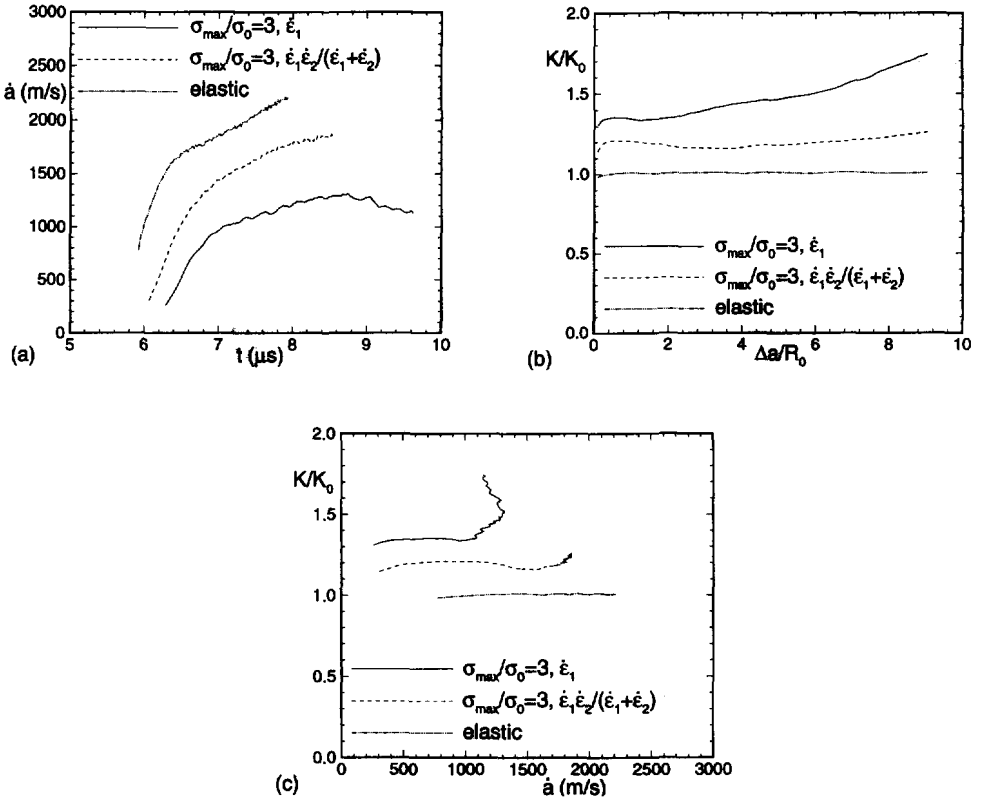

Fig. 8. Comparison of crack growth behavior for three cases; enhanced strain rate hardening with $\sigma_{max} = 3000$ MPa and $\sigma_0 = 1000$ MPa, power law strain hardening with $\sigma_{max} = 3000$ MPa and $\sigma_0 = 1000$ MPa, and an elastic material with $\sigma_{max} = 3000$ MPa. The impact velocity is $V_1 = 10$ m/s. (a) Crack speed, $\dot{a}$, vs time, t. (b) Normalized stress intensity factor, K/K_0, vs normalized crack growth, $\Delta a/R_0$. (c) Normalized stress intensity factor, K/K_0, vs crack speed $\dot{a}$. Results for power law strain rate hardening are denoted by $\dot{\varepsilon}_1$, (15), and results for enhanced strain rate hardening are denoted by $\dot{\varepsilon}_1\dot{\varepsilon}_2/(\dot{\varepsilon}_1+\dot{\varepsilon}_2)$, (16). A value $R_0 = 0.40$ mm is used for normalizing the results of the calculation with elastic material behavior.

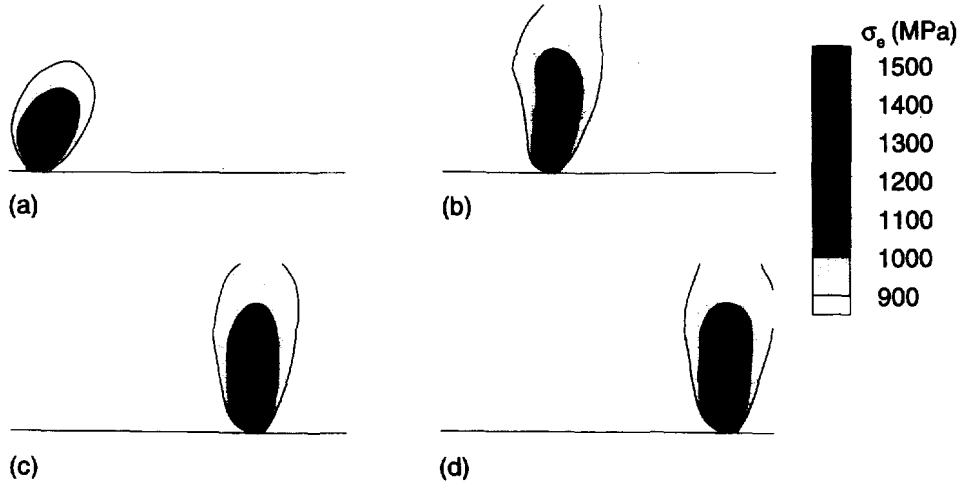

Fig. 9. Contours of Mises effective stress, σ_e, with $\sigma_{max} = 3000$ MPa, $\sigma_0 = 1000$ MPa and enhanced strain rate hardening, (16). The impact velocity is $V_1 = 10$ m/s. The extent of the region shown is 4 mm × 2 mm. (a) $t = 6.0$ μs, $\dot{a} = 0$ m/s. (b) $t = 7.0$ μs, $\dot{a} = 1436$ m/s. (c) $t = 8.0$ μs, $\dot{a} = 1784$ m/s. (d) $t = 8.3$ μs, $\dot{a} = 1835$ m/s.

for the case with enhanced strain rate hardening are much closer in shape and level to those for the elastic material than to those for the material with power law strain rate hardening.

The near-tip strain rates for the power law strain rate hardening and enhanced strain rate hardening materials at this stage of crack growth are compared in Fig. 11. Comparing

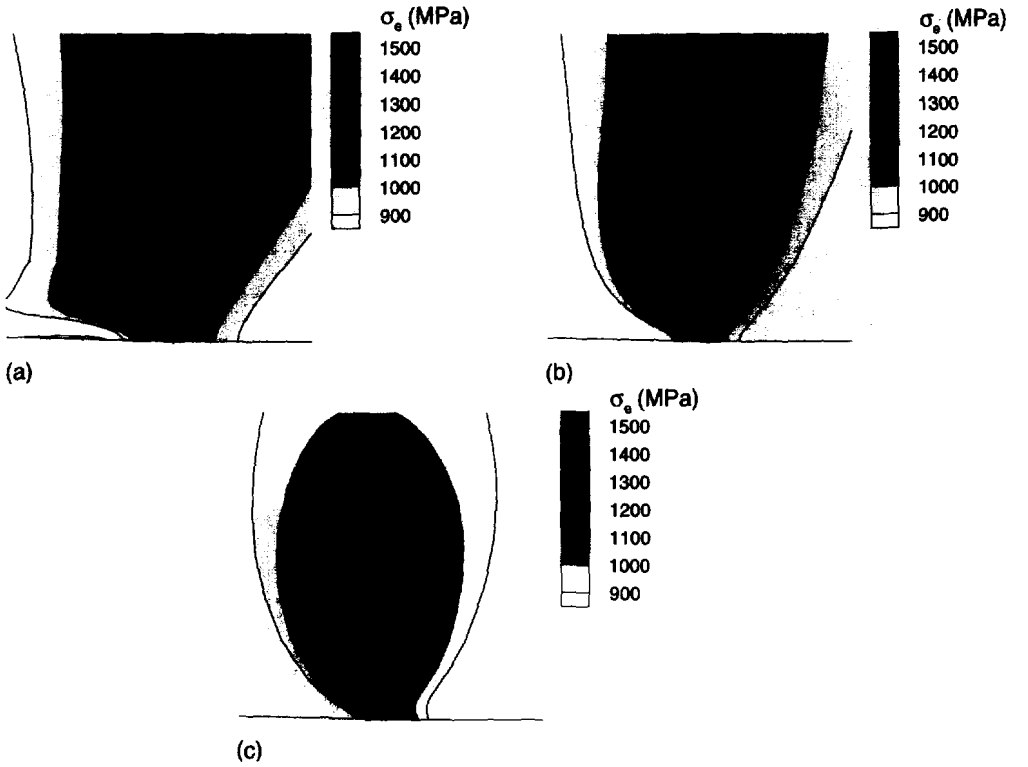

Fig. 10. Contours of Mises effective stress, σ_e, at $\Delta a = 1.8$ mm with $\sigma_{max} = 3000$ MPa. The impact velocity is $V_1 = 10$ m/s. The extent of the region shown is 0.8 mm × 0.8 mm. (a) Power law strain rate hardening and $\sigma_0 = 1000$ MPa ($t = 8.1$ μs, $\dot{a} = 1237$ m/s). (b) Enhanced strain rate hardening and $\sigma_0 = 1000$ MPa ($t = 7.5$ μs, $\dot{a} = 1636$ m/s). (c) Elastic material ($t = 7.0$ μs, $\dot{a} = 1871$ m/s).

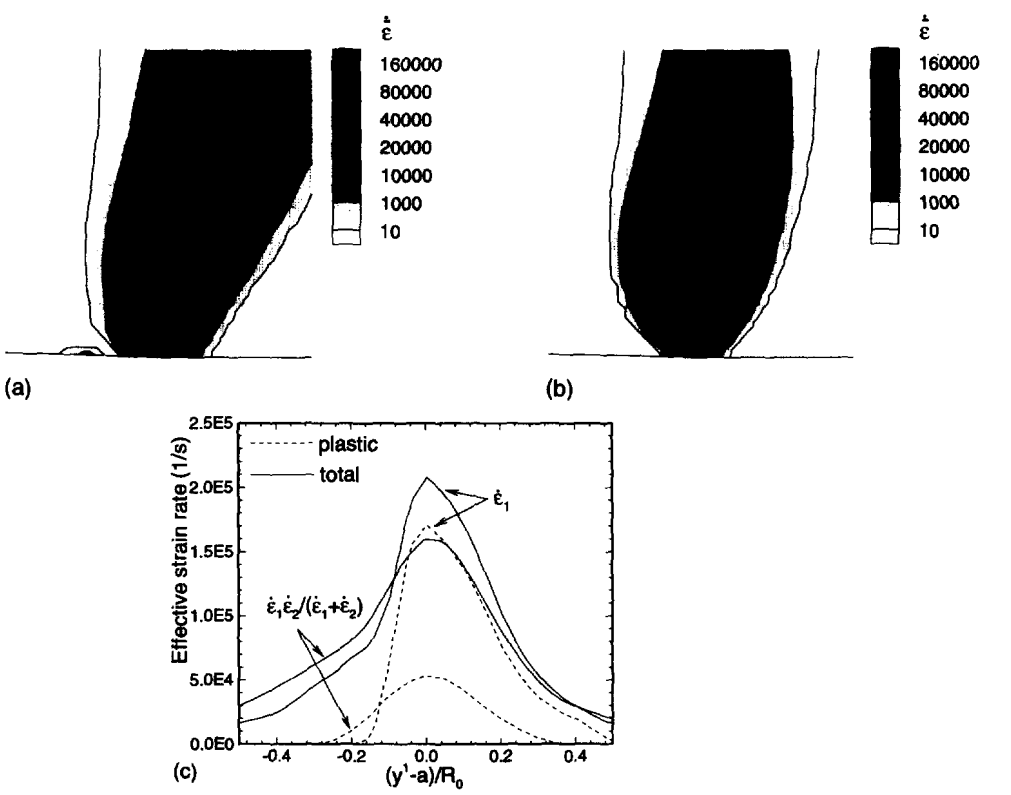

Fig. 11. Contours of the equivalent plastic strain rate, $\dot{\bar{\varepsilon}}$, at $\Delta a = 1.8$ mm for $\sigma_{max} = 3000$ MPa, $\sigma_0 = 1000$ MPa; $V_1 = 10$ m/s. The extent of the region shown is 0.8 mm × 0.8 mm. (a) Power law strain rate hardening ($t = 8.1$ μs, $\dot{a} = 1237$ m/s). (b) Enhanced strain rate hardening ($t = 7.5$ μs, $\dot{a} = 1636$ m/s). (c) Distribution of equivalent plastic and equivalent total strain rate at the crack tip; values are taken at $y^2 = 0.06$ mm above the crack in the deformed configuration.

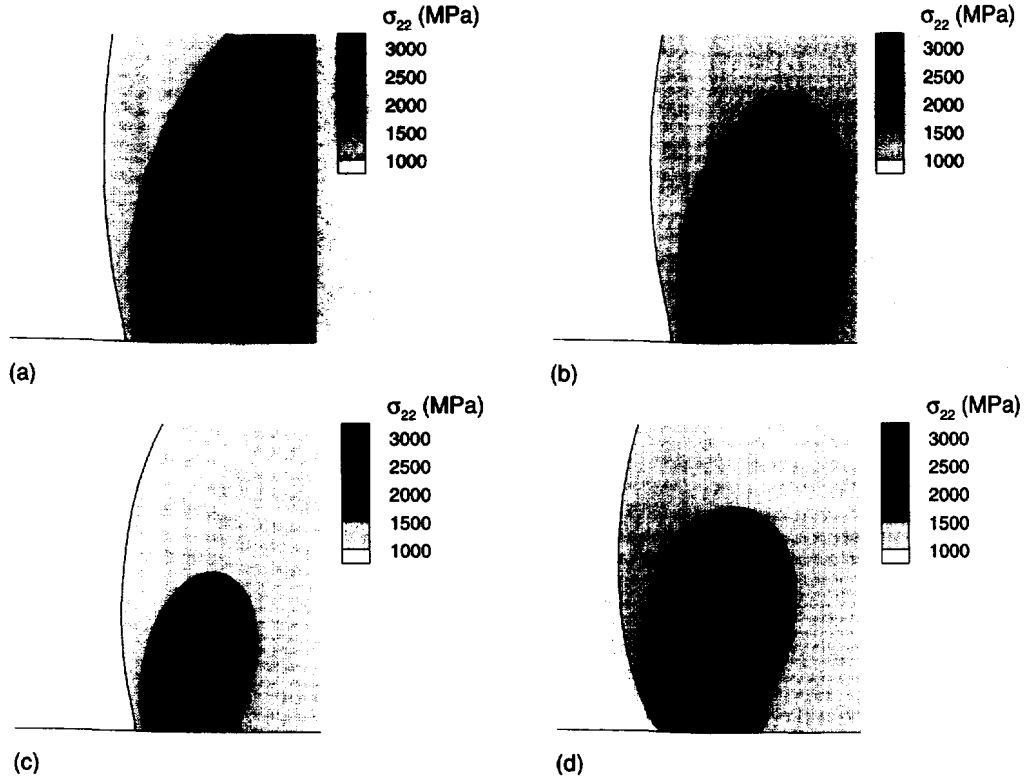

Fig. 12. Contours of the physical component of stress, σ_{22}, at $\Delta a = 1.8$ mm for $\sigma_{max} = 3000$ MPa. The impact velocity is $V_1 = 10$ m/s. The extent of the region shown is 0.8 mm × 0.8 mm. (a) Power law strain rate hardening and $\sigma_0 = 1000$ MPa ($t = 8.1$ μs, $\dot{a} = 1237$ m/s). (b) Enhanced strain rate hardening and $\sigma_0 = 1000$ MPa ($t = 7.5$ μs, $\dot{a} = 1636$ m/s). (c) Elastic material ($t = 7.0$ μs, $\dot{a} = 1871$ m/s). (d) The asymptotic field for a crack in the elastic material for a crack speed of 1871 m/s plotted on the deformed configuration of Fig. 12(c).

Figs 11a and 11b shows the larger plastic strain rates that occur for the power law strain rate hardening material. Evidence of a sector with nearly no plastic strain rate can be seen in Fig. 11a. Also, note the reloading zone behind the current crack tip. Figure 11c shows curves of effective plastic strain rate, $\dot{\bar{\varepsilon}}$ and total effective strain rate, $\dot{\varepsilon}_{eff}$, vs y^1 at $y^2 = 0.06$ mm above the crack plane. The total effective strain rate is defined by

$$\dot{\varepsilon}_{eff} = \sqrt{\tfrac{2}{3}\mathbf{D}:\mathbf{D}}. \tag{25}$$

These curves were obtained from the contour plots in Figs 11a and 11b using facilities in Tecplot. For the power law strain rate hardening material, the curves labeled $\dot{\varepsilon}_1$, the main contribution to the peak total strain rate is the plastic strain rate. On the other hand, for the material with enhanced strain rate hardening, labeled $\dot{\varepsilon}_1\dot{\varepsilon}_2/(\dot{\varepsilon}_1+\dot{\varepsilon}_2)$, the peak strain rate is mainly elastic. In both cases the deformation occurs in a narrow zone at the actual crack tip. In the rate independent, steady state case analyzed by Varias and Shih (1994) a jump was found in the effective plastic strain as a material point passes over the crack tip. Our results, which include strain hardening and two types of strain rate hardening, give high plastic as well as total strain rates in a relatively narrow band.

Contours of the physical stress component σ_{22} at this stage of crack growth are shown in Fig. 12, where

$$\sigma_{22} = \tau^{ij}F_{i2}F_{j2} \tag{26}$$

and τ^{ij} are the contravariant components of Kirchhoff stress on the deformed coordinate net. Because the strain magnitudes remain small, except very near the crack tip, the physical component σ_{22} is not very different from the tensor component τ^{22} over most of the region

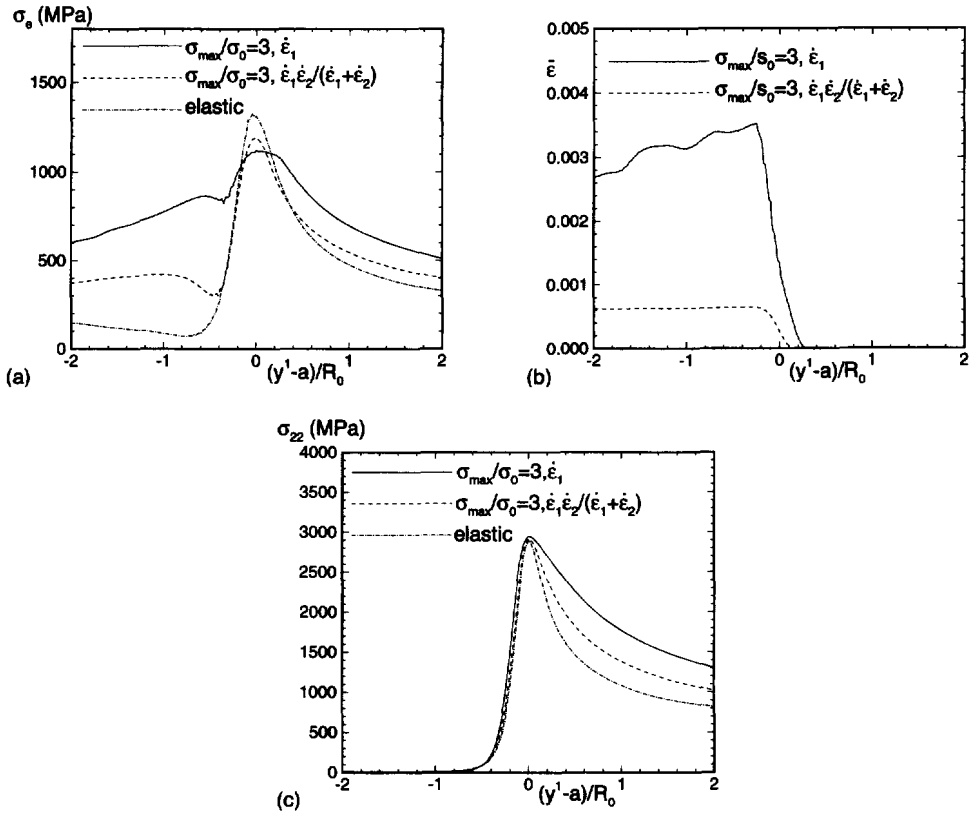

Fig. 13. The distributions of (a) Mises effective stress, σ_e, (b) equivalent plastic strain, $\bar{\varepsilon}$, (c) the physical component of stress, σ_{22}, at the crack tip at $\Delta a = 1.8$ mm and $\sigma_{max} = 3000$ MPa for cases of power law strain rate hardening ($t = 8.1$ μs, $\dot{a} = 1237$ m/s), enhanced strain rate hardening ($t = 7.5$ μs, $\dot{a} = 1636$ m/s) (both with $\sigma_0 = 1000$ MPa) and the elastic material ($t = 7.0$ μs, $\dot{a} = 1871$ m/s); $V_1 = 10$ m/s; values are taken at $y^2 = 0.01$ mm above the crack in the deformed configuration. Results for power law strain rate hardening are denoted by $\dot{\varepsilon}_1$, (15), and results for enhanced strain rate hardening are denoted by $\dot{\varepsilon}_1\dot{\varepsilon}_2/(\dot{\varepsilon}_1+\dot{\varepsilon}_2)$, (16).

shown. For comparison purposes, the asymptotic field for a linear elastic solid is shown in Fig. 12d. The crack speed and the deformed mesh in Fig. 12d are taken to be the same as for the elastic material calculation in Fig. 12c. The stress levels in the asymptotic field in Fig. 12d are noticeably higher than for the calculation in Fig. 12c. This is because the cohesive surface strength of $\sigma_{max} = 3000$ MPa limits the attainable stress level in Fig. 12c. However, the contour shapes are quite similar in these two figures. Furthermore, the distributions for the elastic material, Fig. 12c, and for the material with enhanced strain rate hardening, Fig. 12b, are quite similar.

Figure 13 shows variations of various field quantities with y^1 at a fixed distance ($y^2 = 0.01$ mm) above the crack plane. The variations of Mises effective stress in Fig. 13a show that ahead of the crack the effective stress distribution for the material with enhanced strain rate hardening is much like the distribution for the elastic material; behind the crack the distribution has a shape similar to that for the power law strain rate hardening material, but the level is much lower. As seen in Fig. 13b, the accumulated effective plastic strain, $\bar{\varepsilon} = \int \dot{\bar{\varepsilon}}\, dt$, is reduced by about a factor of four for the material with enhanced strain rate hardening. Note that the plastic strain level is essentially constant behind the current crack tip for the case with enhanced strain rate hardening, although the crack speed is not constant over this interval (see Fig. 8). On the other hand, with power law strain rate hardening, the amount of plastic strain near the current crack tip tends to increase with crack growth. This increase in plastic strain becomes more pronounced when the crack slows down and is particularly enhanced when crack arrest occurs. Figure 13c shows the variations in the physical opening stress component, σ_{22} defined in (26). A log–log regression over the interval $0.2 \geqslant (y^1 - a)/R_0 \geqslant 0.6$ gives a fit to $(y^1 - a)^p$ with p having the values

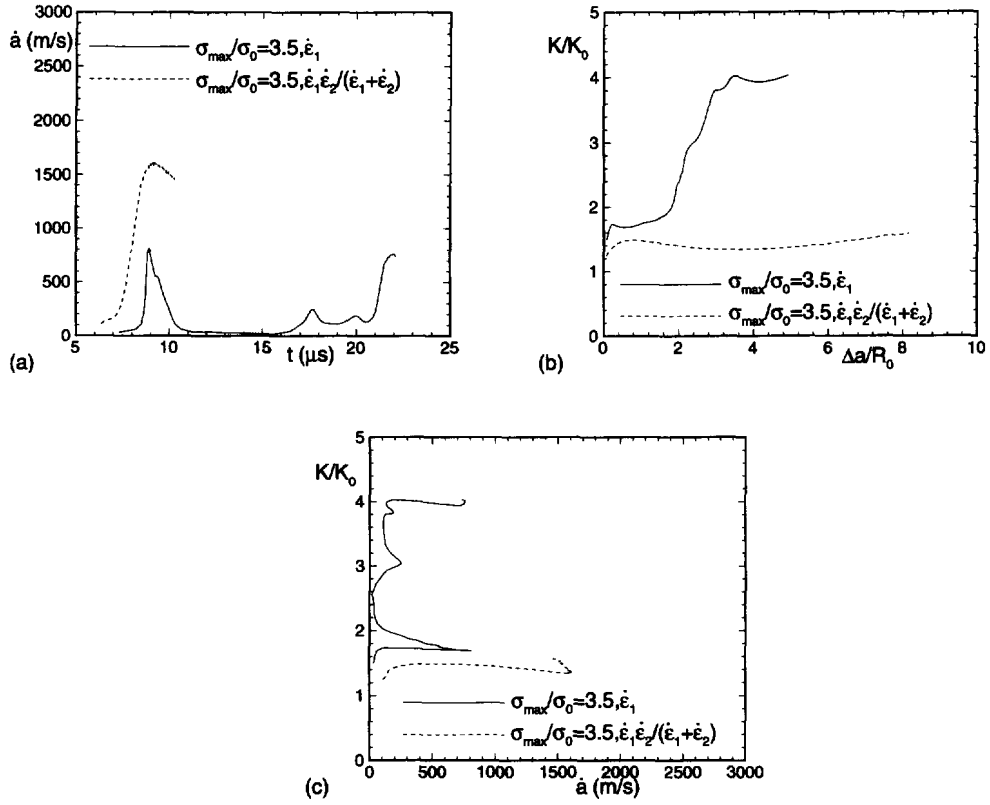

Fig. 14. Comparison of crack growth behavior for two cases; enhanced strain rate hardening $\sigma_{max} = 3500$ MPa and $\sigma_0 = 1000$ MPa, and power law strain rate hardening with $\sigma_{max} = 3500$ MPa and $\sigma_0 = 1000$ MPa. The impact velocity is $V_1 = 10$ m/s. (a) Crack speed, $\dot{a}$, vs time, t. (b) Normalized stress intensity factor, K/K_0, vs normalized crack growth, $\Delta a/R_0$. (c) Normalized stress intensity factor, K/K_0, vs crack speed $\dot{a}$. Results for power law strain rate hardening are denoted by $\dot{\varepsilon}_1$, (15), and results for enhanced strain rate hardening are denoted by $\dot{\varepsilon}_1\dot{\varepsilon}_2/(\dot{\varepsilon}_1+\dot{\varepsilon}_2)$, (16).

$p = -0.41, -0.32, -0.21$ for the elastic case, the enhanced strain rate hardening case and the power law strain rate hardening case, respectively.

Fields for the case with power law rate hardening and $\sigma_{max}/\sigma_0 = 2.0$ (see Fig. 5) are now shown here. Nevertheless, it is worth noting that the contours of Mises effective stress for this case are very similar to the ones depicted in Fig. 10c and the contours of the physical stress component σ_{22} to the ones in Fig. 12c. The size of the active plastic zone, i.e., the region where the plastic strain rate is non-negligible, remains small.

Figures 14–16 show results for a case where the cohesive surface strength is increased to $\sigma_{max} = 3500$ MPa, with $\sigma_0 = 1000$ MPa. Although the ratio $\sigma_{max}/\sigma_0 = 3.5$ is the same as for a calculation shown in Fig. 5 for power law strain rate hardening, $\sigma_0 = 1000$ MPa in Figs 14–16, whereas $\sigma_0 = 857$ MPa in Fig. 5. For the calculations in Figs 14–16, $K_0 = 66$ MPa$\sqrt{\text{m}}$ and $R_0 = 0.46$ mm. With power law strain rate hardening, crack arrest occurs in Fig. 14a, with crack growth resuming after the arrival of the second loading wave. There is a delay between the arrival of the second loading wave at $t = 14.94$ μs and the resumption of crack growth. The increase in crack speed at $t \approx 20.5$ μs occurs before the third loading wave arrives at $t = 24.9$ μs. With the enhanced strain rate hardening relation in Fig. 2, a maximum crack speed is attained at nearly the same time as at the first peak for the power law strain rate hardening material. However, crack arrest does not occur over the range of crack growth computed (the computation is terminated when the crack approaches the end of the uniform mesh region). Plots of the normalized stress intensity factors versus crack extension are shown in Fig. 14b. For the material with power law strain rate hardening, a large increase in K accompanies crack arrest. The value of K at which crack growth reinitiates with the second loading wave is about 2.5 times larger than the value of K at the initiation of crack growth. In A533-B steel specimens, Bonenberger and Dally (1995) have

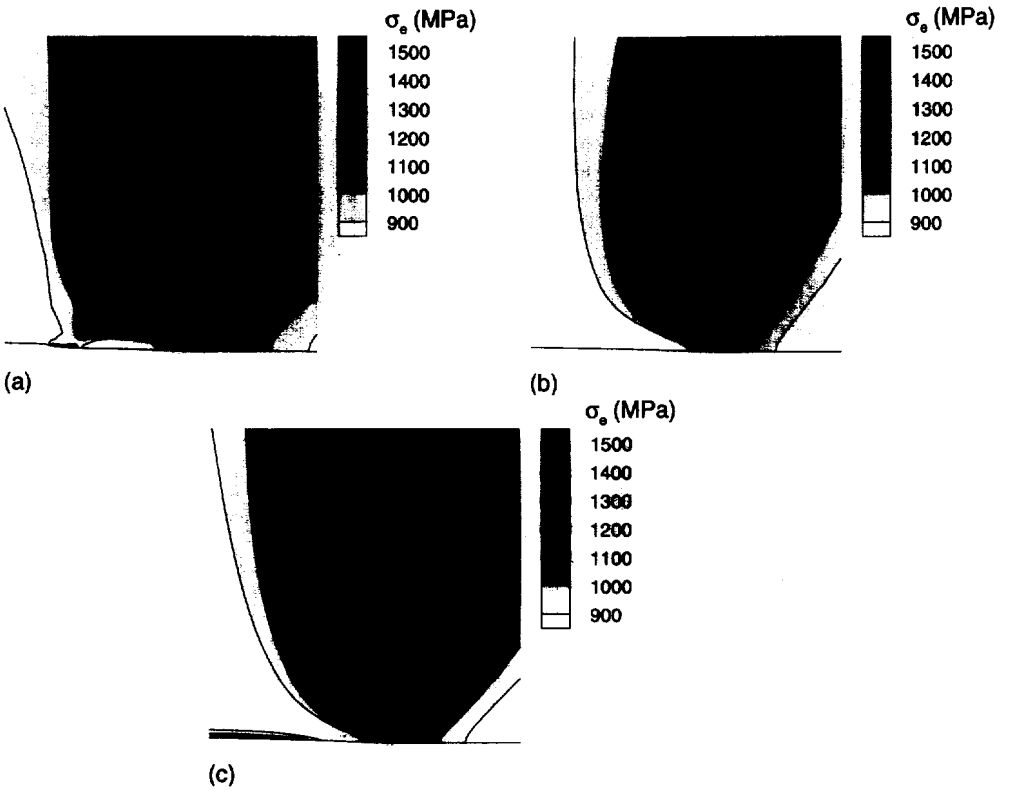

Fig. 15. Contours of Mises effective stress, σ_e, with $\sigma_{max} = 3500$ MPa and $\sigma_0 = 1000$ MPa. The impact velocity is $V_1 = 10$ m/s. The extent of the region shown is 0.93 mm × 0.93 mm. (a) Power law strain rate hardening at $t = 9.0$ μs ($\Delta a = 0.32$ mm, $\dot{a} = 750$ m/s). (b) Enhanced strain rate hardening at $t = 9.0$ μs ($\Delta a = 1.85$ mm, $\dot{a} = 1595$ m/s). (c) Enhanced strain rate hardening at $t = 10.0$ μs ($\Delta a = 3.43$ mm, $\dot{a} = 1509$ m/s).

found that the K value for crack reinitiation is substantially greater than the crack arrest value. The results in Fig. 14 are consistent with this observation.

Contours of Mises effective stress are shown in Fig. 15 for the power law strain rate hardening material at $t = 9.0$ μs, Fig. 15a, and for the material with the enhanced strain rate hardening at $t = 9.0$ μs, Fig. 15b, and at $t = 10.0$ μs, Fig. 15c. Because of the very different crack growth histories, the crack extension at $t = 9.0$ μs is $\Delta a = 0.32$ mm for the power law rate hardening material with $\Delta a = 1.85$ mm at $t = 9.0$ μs and $\Delta a = 3.43$ mm at $t = 10.0$ μs for the material with enhanced strain rate hardening. Contours for the power law material in Fig. 15a show a region of relatively high Mises effective stress behind the current crack tip. For the material with enhanced strain rate hardening such a region is not present at $t = 9.0$ μs, while at $t = 10.0$ μs, which corresponds to decreasing crack speed, such a region has formed. The Mises effective stress levels are also much higher for the material with enhanced strain rate hardening, Figs 15b and 15c.

Figure 16 shows corresponding contours of effective plastic strain rate. For the material with enhanced strain rate hardening a zone of secondary plastic loading behind the crack tip is formed only at decreasing crack speed, Fig. 16c. In Fig. 16b, which is at a stage where the crack speed is increasing, the contours of effective plastic strain rate are similar to those in Fig. 10b. The plots in Fig. 16d show that the effective plastic strain rate is nearly the same as the total effective strain rate for the material with power law strain rate hardening, whereas for the material with enhanced strain rate hardening, the main contribution to the total strain rate is the elastic one. This changes only a little with the formation of the secondary zone with significant plastic straining.

Balance of energy requires the work of the applied loading to equal the sum of the kinetic energy of the material, the elastic energy stored in the material, the plastic dissipation and the cohesive surface energy. The relative magnitudes of the last two contributions, the plastic dissipation ($\int \boldsymbol{\tau} : \mathbf{D}^p \, dt$) and the cohesive surface energy, (19), are plotted against the

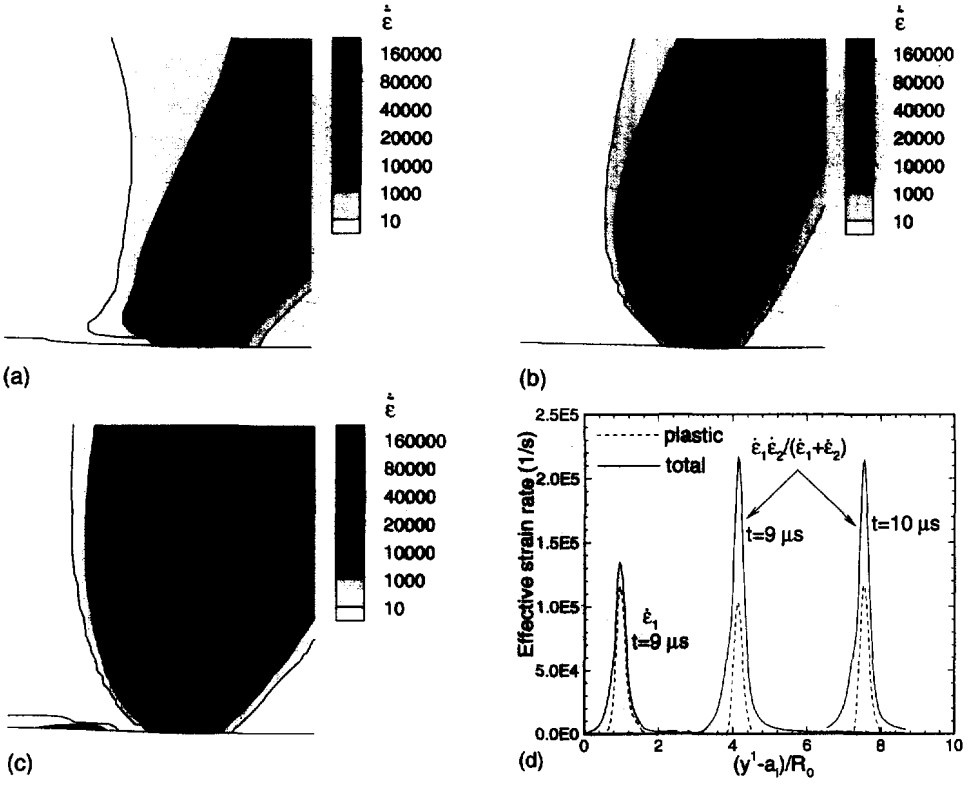

Fig. 16. Contours of equivalent plastic strain rate, $\dot{\bar{\varepsilon}}$, with $\sigma_{max} = 3500$ MPa and $\sigma_0 = 1000$ MPa. The impact velocity is $V_1 = 10$ m/s. The extent of the region shown is 0.93 mm × 0.93 mm. (a) Power law strain rate hardening at $t = 9.0$ μs ($\Delta a = 0.32$ mm, $\dot{a} = 750$ m/s). (b) Enhanced strain rate hardening at $t = 9.0$ μs ($\Delta a = 1.85$ mm, $\dot{a} = 1592$ m/s). (c) Enhanced strain rate hardening at $t = 10.0$ μs ($\Delta a = 3.43$ mm, $\dot{a} = 1509$ m/s). (d) Distribution of equivalent plastic strain rate and equivalent total strain rate at the crack tip. Values are taken at $y^2 = 0.06$ mm above the crack in the deformed configuration.

amount of crack growth in Fig. 17 for four cases; $\sigma_{max}/\sigma_0 = 3.0$ and $\sigma_{max}/\sigma_0 = 3.5$, with both power law and enhanced strain rate hardening for each value of σ_{max}/σ_0. The energy values in Fig. 17 are for a metre thickness and pertain to the quarter of the specimen analyzed numerically. With enhanced strain rate hardening and $\sigma_{max}/\sigma_0 = 3.0$, the cohesive energy is somewhat larger than the plastic dissipation. With power law strain rate hardening and $\sigma_{max}/\sigma_0 = 3.0$, the plastic dissipation exceeds the cohesive energy in the latter stages of crack growth. This is similar for the calculation with enhanced strain rate hardening and $\sigma_{max}/\sigma_0 = 3.5$. However, with power law strain rate hardening and $\sigma_{max}/\sigma_0 = 3.5$ the plastic dissipation exceeds the cohesive energy by an order of magnitude. This is the case for which crack arrest occurs.

4. DISCUSSION

Dynamic crack growth has been analyzed using a framework where the crack growth history is a direct outcome of the analysis, determined by the cohesive surface properties (the strength and the work of separation), by the material properties and by the imposed loading. In the calculations here, the crack has been restricted to grow along the initial crack line. The focus has been on the effect of strain rate hardening on crack growth and arrest under dynamic loading conditions. With material properties taken to be representative of a structural steel, a crack speed is reached at which the effective stress intensity factor increases dramatically. This crack speed, which depends on the loading as well as on material and cohesive properties, essentially serves as a limiting crack speed.

This can be contrasted with the case of an elastic solid where, for straight ahead crack growth, the Rayleigh wave speed is the limiting crack speed, e.g., Freund (1990), and crack

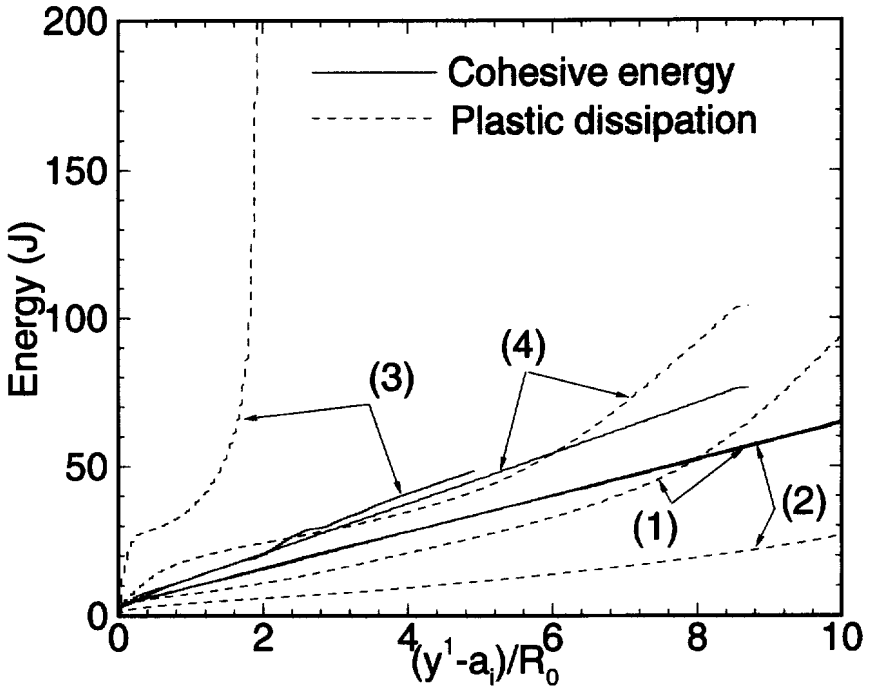

Fig. 17. The cohesive energy and the plastic dissipation (1 m thickness) as functions of normalized crack growth for (1) Power law strain rate hardening with $\sigma_{max} = 3000$ MPa and $\sigma_0 = 1000$ MPa; (2) Enhanced strain rate hardening with $\sigma_{max} = 3000$ MPa and $\sigma_0 = 1000$ MPa; (3) Power law strain rate hardening with $\sigma_{max} = 3500$ MPa, $\sigma_0 = 1000$ MPa; (4) Enhanced strain rate hardening with $\sigma_{max} = 3500$ MPa and $\sigma_0 = 1000$ MPa.

branching leads to attainable crack speeds in isotropic elastic solids being less than the Rayleigh wave speed, as in Xu and Needleman (1994).

The course of crack growth in plastic or viscoplastic solids is, to a large extent, set by the dissipation accompanying inelastic deformation. A key parameter is the ratio of the material flow strength to the cohesive surface strength, Needleman (1990b), Tvergaard and Hutchinson (1992). Assuming that the cohesive properties are independent of temperature and that the main effect of a temperature change is through its effect on the flow strength, Fig. 5 can be viewed as illustrating the effect of specimen temperature on dynamic crack growth. Increasing values of σ_{max}/σ_0 correspond to increasing temperature. At very low temperatures, macroscopic plasticity makes a negligible contribution to the effective toughness, so that the macroscopic toughness directly measures the resistance associated with the separation process. At higher temperatures, illustrated by the results for $\sigma_{max}/\sigma_0 = 3.0$, the apparent toughness increases substantially. With a further increase in temperature, the crack arrests after some initial crack growth. A ductile–brittle transition is generally associated with a change in fracture mechanism, with plastic void growth being the ductile fracture mechanism and cleavage the brittle fracture mechanism. Analyses using physically based models for these two mechanisms reproduce the observed transition, e.g., Tvergaard and Needleman (1993), Needleman and Tvergaard (1995), Gao *et al.* (1996). Here, although a change in mechanism is not modeled, the results in Fig. 5 suggest a ductile–brittle transition for dynamic crack growth simply arising from the decrease in flow strength with increasing temperature, even with the material characterized as power law strain rate hardening. On the other hand, at a fixed temperature, i.e., at a fixed value of the flow strength σ_0, and with the loading rate varied, whether the strain rates at the crack tip are within the power law or enhanced strain rate hardening regime plays a major role in determining ductile (high toughness) versus brittle (low toughness) response.

The enhanced strain rate hardening at high strain rates leads to less plastic straining and therefore to a more brittle response, Fig. 8 and Fig. 14; crack speeds are higher and the effective toughness is reduced. The enhanced strain rate hardening also gives rise to higher near tip stress levels. As a consequence, a higher toughness is required for crack

arrest, Fig. 14. For power law viscous materials, the fields at a growing crack undergo a change in character at rate exponents m in (15) equal to 1/3; for values of m less than 1/3 the near tip fields are the HRR fields, Hutchinson (1968) Rice and Rosengren (1968), whereas for m greater than 1/3 the near tip fields are the elastic singular fields, Hui and Riedel (1981) for quasi-static growth and Lo (1983) for dynamic growth. The viscoplastic flow rule used in the present calculations is history dependent and the near tip-fields are not quite the same as the elastic near-tip fields. Nevertheless, a similar transition occurs, with plastic strain rates dominating in the low rate regime and elastic strain rates dominating in the high rate regime, where the strain rate hardening is much greater. Furthermore, the stress distributions become more like those for an elastic growth crack than for the power law rate hardening material. The dominance of elastic strain rates and a change in the character of the crack tip fields to the elastic fields are key assumptions of the analysis of dynamic crack growth in Freund and Hutchinson (1985). Our analyses suggest that these are reasonable approximations in the enhanced strain rate hardening regime.

Regardless of the strain rate hardening description, a feature in most of our calculations for viscoplastic solids is that the crack speed increases, reaches a maximum and then decreases. This crack speed maximum is associated with the development of a region of increased Mises effective stress, Figs 7d, 10a, 15c. When a maximum does not occur, as for the calculation with $\sigma_{max}/\sigma_0 = 2.0$ in Fig. 5 and for the case with enhanced strain rate hardening in Fig. 8, a region behind the current crack tip with increased Mises effective stress does not develop.

The results for pure power law strain hardening can be regarded as having been obtained for a relation of the form in Fig. 2, but where the transition strain rate is greater than the strain rates occurring anywhere in the material. Thus, the comparison between the materials with power law strain rate hardening and enhanced strain rate hardening illustrates circumstances where strain rates are below and above the transition strain rate, respectively. This comparison is particularly interesting in Fig. 14, where crack arrest occurs for the power law rate hardening material but not for the material with enhanced strain rate hardening. Thus, whether or not crack growth rates are fast enough for the near-tip material to enter the enhanced strain rate hardening regime may be a significant factor in determining if crack arrest occurs.

Under quasi-static conditions, crack growth in a plastic solid with strain hardening characteristics like those used here can only occur for values of the cohesive strength up to 3.5–4.0 σ_0; higher values of the cohesive strength essentially preclude crack growth, Tvergaard and Hutchinson (1992). For fast cracks, continued crack growth is possible for higher values of the cohesive strength if the crack speed is large enough for the material in the crack tip region to enter the regime where enhanced strain rate hardening comes into play. This suggests, at least within the framework of this cohesive surface model, that if a crack initiates in a weak region or brittle phase, attaining a crack speed fast enough for enhanced strain rate hardening may be necessary for crack propagation to continue into the tougher region or more ductile phase.

Acknowledgements—We are pleased to acknowledge support from the Air Force Office of Scientific Research under Grant F49620-94-0300. T.S. is also grateful for the support provided by Schrödinger Fellowship J00994—TEC, FWF Vienna, Austria. The computations reported on here were carried out on the Cray C90 at the Pittsburgh Supercomputer Center.

REFERENCES

Brickstad, B. and Nilsson, F. (1980) Numerical evaluation by FEM of crack propagation experiments. *International Journal of Fracture* **16**, 71–84.

Belytschko, T., Chiapetta, R. L. and Bartel, H. D. (1976) Efficient large scale non-linear transient analysis by finite elements. *International Journal of Numerical Methods in Engineering* **10**, 579–596.

Bonenberger, R. J. and Dally, J. W. (1995) On improvements in measuring crack arrest toughness. *International Journal of Solids and Structures* **32**, 897–909.

Campbell, J. D. and Ferguson, W. G. (1970) The temperature and strain-rate dependence of the shear strength of mild steel. *Philosophical Magazine* **21**, 63–82.

Freund, L. B. (1990) *Dynamic Fracture Mechanics*, Cambridge University Press, Cambridge.

Freund, L. B. and Hutchinson, J. W. (1985) High strain-rate crack growth in rate-dependent plastic solids. *Journal of Mechanics and Physics of Solids* **33,** 169–191.

Gao, X., Shih, C. F., Tvergaard, V. and Needleman, A. (1996) Constraint effects on the ductile–brittle transition in small scale yielding. *Journal of Mechanics and Physics of Solids* (submitted).

Hui, C. Y. and Riedel, H. (1981) The asymptotic stress and strain field near the tip of a growing crack under creep conditions. *International Journal of Fracture* **17,** 409–425.

Hutchinson, J. W. (1968) Singular behavior at the end of a tensile crack in a hardening material. *Journal of Mechanics and Physics of Solids* **16,** 13–31.

Klopp, R. W., Clifton R. J. and Shawki, T. G. (1985) Pressure–shear impact and the dynamic plastic response of metals. *Mechanics of Materials* **4,** 375–385.

Krieg, R. D. and Key, S. W. (1973) Transient shell response by numerical time integration. *International Journal of Numerical Methods in Engineering* **7,** 273–286.

Lam, P. S. and Freund, L. B. (1985) Analyses of dynamic growth of a tensile crack in an elastic-plastic material. *Journal of Mechanics and Physics of Solids* **33,** 153–167.

Lee, Y. and Prakash, V. (1995) Dynamic fracture toughness of 4340 VAR steel under conditions of plane strain. *Metal Material Transactions A* **26A,** 2527–2543.

Lo, K. K. (1983) Dynamic crack-tip fields in rate-sensitive solids. *Journal of Mechanics and Physics of Solids* **31,** 287–305.

Mataga, P. A., Freund, L. B. and Hutchinson, J. W. (1987) Crack tip plasticity in dynamic fracture. *Journal of Physics and Chemistry of Solids* **48,** 985–1005.

Nakamura, T., Shih, C. F. and Freund, L. B. (1985) Computational methods based on an energy integral in dynamic fracture. *International Journal of Fracture* **27,** 229–243.

Needleman, A. (1987) A continuum model for void nucleation by inclusion debonding. *Journal of Applied Mechanics* **54,** 525–531.

Needleman, A. (1990a) An analysis of decohesion along an imperfect interface. *International Journal of Fracture* **42,** 21–40.

Needleman, A. (1990b) An analysis of tensile decohesion along an interface. *Journal of Mechanics and Physics of Solids* **38,** 289–324.

Needleman, A. and Tvergaard, V. (1991) An analysis of dynamic, ductile crack growth in a double edge cracked specimen. *International Journal of Fracture* **49,** 41–67.

Needleman, A. and Tvergaard, V. (1995) Analysis of a brittle–ductile transition under dynamic shear loading. *International Journal of Solids and Structures* **32,** 2571–2590.

Peirce, D., Shih, C. F. and Needleman, A. (1984) A tangent modulus method for rate dependent solids. *Computers and Structures* **18,** 875–887.

Rice, J. R. (1968) A path independent integral and the approximate analysis of strain concentration by notches and cracks. *Journal of Applied Mechanics* **35,** 379–386.

Rice, J. R. and Rosengren, G. F. (1968) Plane strain deformation near a crack tip in a power law hardening material. *Journal of Mechanics and Physics of Solids* **16,** 1–12.

Rosakis, A. J. and Zehnder, A. T. (1985) On the dynamic fracture of structural metals. *International Journal of Fracture* **27,** 169–186.

Rose, J. H., Ferrante, J. and Smith, J. R. (1981) Universal binding energy curves for metals and bimetallic interfaces. *Physics Review Letters* **47,** 675–678.

Siegmund, T. and Needleman, A. (1996) Numerical studies of fast crack growth in elastic-plastic solids. In *Proc. IUTAM Symp. Nonlinear analysis of fracture* (ed. J. R. Willis), Cambridge, to be published.

Tvergaard, V. and Hutchinson, J. W. (1992) The relation between crack growth resistance and fracture process parameters in elastic-plastic solids. *Journal of Mechanics and Physics of Solids* **40,** 1377–1397.

Tvergaard, V. and Needleman, A. (1993) An analysis of the brittle–ductile transition in dynamic crack growth. *International Journal of Fracture* **59,** 53–67.

Varias, A. G. and Shih, C. F. (1994) Dynamic steady crack growth in elastic-plastic solids-propagation of strong discontinuities. *Journal of Mechanics and Physics of Solids* **42,** 1817–1848.

Xu, X.-P. and Needleman, A. (1994) Numerical simulations of fast crack growth in brittle solids. *Journal of Mechanics and Physics of Solids* **42,** 1397–1434.

Zehnder, A. T. and Rosakis, A. J. (1990) Dynamic fracture initiation and propagation in 4340 steel under impact loading. *International Journal of Fracture* **43,** 271–285.

Zhou, M., Needleman, A. and Clifton, R. J. (1994) Finite element simulation of shear localization in plate impact. *Journal of Mechanics and Physics of Solids* **42,** 423–458.